Materials and Design 188 (2020) 108488

Contents lists available at ScienceDirect

Materials and Design

journal homepage: www.elsevier.com/locate/matdes

Computational and experimental characterization of 3D-printed PCL structures toward the design of soft biological tissue scaffolds

Hailong Liu [a,c,*], Astrid Ahlinder [a], Mohammed A. Yassin [b], Anna Finne-Wistrand [a], T. Christian Gasser [c]

[a] Department of Fibre and Polymer Technology, KTH Royal Institute of Technology, Stockholm, Sweden
[b] Department of Clinical Dentistry, University of Bergen, Bergen, Norway
[c] Department of Solid Mechanics, KTH Royal Institute of Technology, Stockholm, Sweden

HIGHLIGHTS

- A numerical model was constructed to investigate the effect of meso-structure on mechanical and transport properties of scaffold.
- The designed meso-structures for scaffolds were adequately realized via 3D printing.
- The computed scaffold stiffness under compression loading agrees well with experimental results.
- The gradient&staggered design resulted in a low scaffold stiffness (~ 1 MPa).
- The properties of 3D-printed poly (ε-caprolactone) scaffolds can be tuned via meso-structures toward soft tissue engineering.

GRAPHICAL ABSTRACT

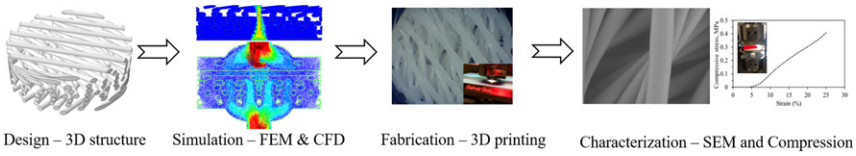

ARTICLE INFO

Article history:
Received 20 November 2019
Received in revised form 7 January 2020
Accepted 8 January 2020
Available online 10 January 2020

Keywords:
Scaffold
3D printing
Meso-structure
Finite element analysis
Computational fluid dynamics
Soft tissue engineering

ABSTRACT

Degradable porous polymeric structures are attractive candidates for biological tissue scaffolds, and adequate mechanical, transport, chemical and biological properties determine their functionality. Aside from the properties of polymer-based materials, the scaffold's meso-structure controls its elasticity at the organ length-scale. This study investigated the effect of the meso-structure on scaffolds' mechanical and transport properties using finite element analysis (FEA) and computational fluid dynamics (CFD). A number of poly (ε-caprolactone) (PCL) - based scaffolds were 3D printed, analyzed by microcomputed tomography (micro-CT) and mechanically tested. We found that the gradient (G) and gradient and staggered (GS) meso-structure designs led to a higher scaffold permeability, a more homogeneous flow inside the scaffold, and a lower wall shear stress (WSS) in comparison with the basic (B) meso-structure design. The GS design resulted in scaffold stiffness as low as 1.07/0.97 MPa under compression/tension, figures that are comparative with several soft tissues. Image processing of micro-CT data demonstrated that the imposed meso-structures could have been adequately realized through 3D printing, and experimental testing validated FEA analysis. Our results suggest that the properties of 3D-printed PCL-based scaffolds can be tuned via meso-structures toward soft tissue engineering applications. The biological function of designed scaffolds should be further explored in-situ studies.

* Corresponding author at: Department of Fibre and Polymer Technology, KTH Royal Institute of Technology, Stockholm, Sweden.
E-mail address: hailongl@kth.se (H. Liu).

https://doi.org/10.1016/j.matdes.2020.108488

1. Introduction

Degradable polymeric porous three-dimensional (3D) structures, scaffolds, have been widely explored as a promising way for the repair and regeneration of damaged biological tissues [1–3]. A scaffold should ideally substitute the naive extracellular matrix (ECM), thereby provides structural support for cell migration, tissue formation and remodeling [4–6]. The scaffolds therefore aim at mimicking the structure and function of native ECM toward the presentation of biological cues able to regulate cell activities. Such functionality critically depends on adequate mechanical, transport, chemical and biological scaffold properties [7–10].

Additive manufacturing (AM), often referred to as 3D printing, has become a very popular technique in the production of scaffolds. It provides design freedom and supports the fabrication of complicated geometries with controlled interconnectivity and porosity [11–15]. Fused filament fabrication (FFF) is an extrusion-based manufacturing technique in which filaments are melted through the heated extruder. The object is then created layer by layer on the printer bed [16]. Given its wide accessibility and low costs, this technology is often used in the fabrication of polymer-based scaffolds. It enables control of the 3D scaffold's properties through the variation of structural parameters, such as strand diameter, space and alignment by taking the polymeric properties into account [17–23].

Degradable aliphatic polyesters such as poly (ε-caprolactone) (PCL) with its copolymers have a long history for usage within medical devices and as scaffold substrates within tissue engineering [12,24–28]. The semi-crystalline poly (ε-caprolactone) (PCL) is one of the most well-used polyesters owing to its long term mechanical stability but also a low melting point and high thermal stability allowing for a wide processing window in a range of 3D printing techniques [27,29–32]. Given PCL's relatively high stiffness of 300 to 500 MPa, matching the elasticity of native soft biological tissues with 3D-printed scaffolds are challenging in comparison with other conventional techniques, such as salt leaching [33].

However, scaffold mechanical properties can be tuned through different designs of internal 3D structures. There are several design methods that have been proposed in the literature. Among them, computer assisted design (CAD) based method has been mainly used to construct 3D simple geometries combining standard primitives (cubes, spheres, cylinders, etc.) through Boolean operations. The dimension, porosity, and mechanical properties of the scaffold can be controlled by repeating these unit cells in a periodic manner [34–36]. Imaged-based design represents an alternative approach, which combines imaging processing and design software with solid free-form fabrication technology. This method allows to rapidly modeling scaffold structures toward a specific application in both macro and micro length scales [37–39]. However, the high resolution of scaffold microstructures may limit the choice of the fabrication materials. Another alternative method is implicit surface modeling (ISM), which allows scaffold structures to be described using mathematic functions. The scaffolds based on triply periodic minimal surfaces (TPMS) have shown a high surface-to-volume ratio and positive effects on cell migration and tissue ingrowth [40–42]. However, ISM based scaffolds often have a relative high stiffness, which might not be a suitable option for soft tissue engineering applications. The aforementioned methods can hardly be coupled to extrusion-based manufacturing techniques (e.g. FFF, Bioplotter). A feasible method, namely space-filling curves, has been used for polymeric scaffolds manufactured based on FFF technique. In this method, the scaffold structure is generated in a layer-by-layer fashion from a predefined pattern. For these polymeric scaffolds, the porosity is known to have a major impact on the scaffold elasticity [12,43–45]. Other works point out that structural parameters, such as strand orientation, strand space, strand diameter also influence scaffold mechanical properties [46–48]. To be specific, the compressive modulus reduces along with the change of the strand orientation from 0/60/120° to 0/72/144/36/108°, as well as from 90° to 45° [47,48].

The scaffold's structure at the length-scale of approximately 1 mm (meso-structure) controls its elasticity at the organ length-scale [49]. Organ function determines the native mechanical properties of soft biological tissues. The elastic moduli range from Pascals for brain tissue and kilo-Pascals for nerves, breast tissue, skin and vessels, to mega-Pascals for heart valves and tendons [50–56]. Consequently, scaffolds with elastic moduli as low as 1 MPa are attractive for soft tissue engineering applications.

Aside from its mechanical properties, the scaffold's meso-structure also influences factors such as the transport of nutrients, adhesion of cells and deposition of ECM compounds. While an integral understanding of interactions remains to be developed, some isolated aspects have already been reported. It is known that the porosity and pore morphology of a scaffold determines its permeability, and thus the capacity to conduct fluid flow. Fluid flow is a main determinant of the transport of oxygen, nutrients and waste products, factors that are crucial to the ingrowth of cells and the regeneration of biological tissues. This may also explain why porosity and pore morphology strongly correlate with the seeding, proliferation and differentiation of cells [9,11,57–61], and why a low permeability increases cellular proliferation for chondrocytes, while a high permeability promotes cellular differentiation for bone marrow stromal cells [62]. The scaffold's meso-structure also affects the distribution and magnitude of flow-induced wall shear stress (WSS), factors known to impact cell density [63–65]. Most interestingly, a spatial pore size gradient improves cell seeding and cell distribution in comparison with a homogenous pore size distribution [43,66,67].

The present study aims at tailoring mechanical and transport properties for 3D-printed PCL scaffolds through different structure designs for soft biological tissue applications. Thus our meso-structures were designed toward a low elastic scaffold modulus. Finite element analysis (FEA) and computational fluid dynamics (CFD) were used to predict the mechanical and transport properties of the individual scaffold structures in a pre-manufactured design phase. A number of PCL-based scaffolds were then 3D printed, analyzed by microcomputed tomography (micro-CT) and scanning electron microscopy (SEM) as well as mechanically tested. The acquired data was used to validate the computational scaffold models proposed in this study.

2. Materials and methods

2.1. Scaffold structure design

This study investigated layered 3D-printed scaffolds, and thus meso-structures that are formed by placing a number of layers on top of each other. Our meso-structures were parameterized by four design parameters: strand orientation (SO), strand space (SS), strand diameter (SD) and strand length (SL). Fig. 1 illustrates the meso-structures, and Table 1 summarizes the design parameters of the ten scaffolds investigated in this study. The studied designs may be grouped into three distinct families: basic (B), gradient (G), gradient and staggered (GS) meso-structures. All scaffolds were formed by nine layers and the strand diameter of SD = 0.4 mm. Other structural parameters may differ between the layers, as detailed below.

B design: SL and SS were constant, while SO continuously changed from layer to layer.

G design: SL was constant, while SS and SO continuously changed from layer to layer. The change of SS leads to a gradient of pore size across the scaffold's thickness direction (Z-axis).

GS design: SL was constant, while SS and SO continuously changed from layer to layer. However, in comparison with the B or G design, the strands were shorter and partially overlapped; see Fig. 1(b). The staggered arrangement of strands avoids the direct mechanical communication along the strand's direction.

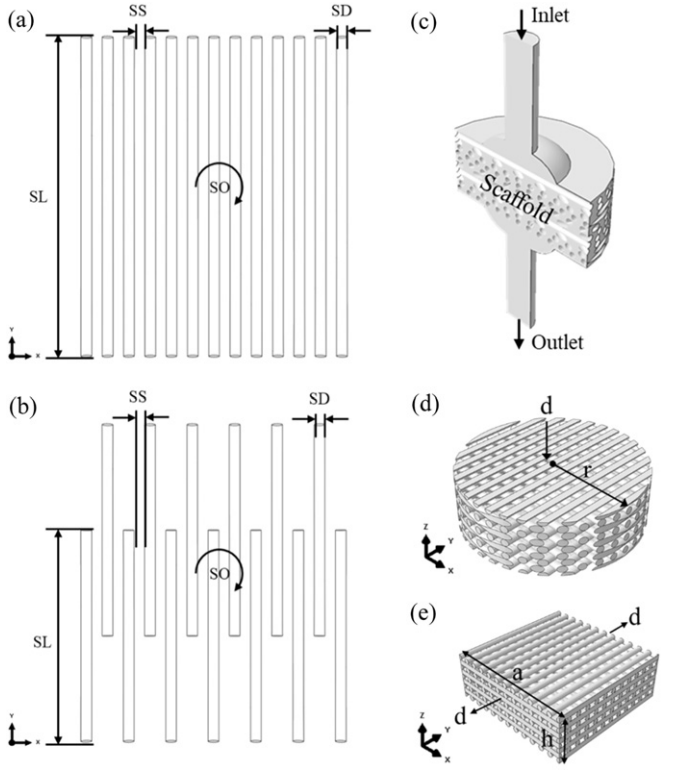

Fig. 1. Schematic illustration of scaffold designs. (a) Building unit for the basic (B) and gradient (G) meso-structures. (b) Building unit for the gradient and staggered (GS) meso-structure. (c) Geometric representation of the computational domain of the virtual bioreactor investigated by computational fluid dynamics (CFD) simulations. (d) Prescription of the displacement *d* toward loading the scaffold in compression. (e) Prescription of the displacement *d* toward loading the scaffold in tension. Abbreviations: SD: strand diameter; SL: strand length; SO: strand orientation; SS: strand space.

Table 1 lists the theoretical porosity in percent of these scaffold designs,

$$p = 100(1-V_{\text{strands}})/V_{\text{total}} \tag{1}$$

where V_{total} and V_{strands} denote the total volume and the strands' volume, respectively.

Given a specific meso-structure, cylinder-shaped scaffolds (10 mm in diameter) and cuboid-shaped scaffolds (9.8 mm edge length) were designed; see Fig. 1(d, e). Both geometries were nine layers, and thus 3.6 mm thick. The cylindrical scaffolds were used to simulate scaffold compression and water transport through them, while the cuboidal scaffolds were used to simulate the scaffolds' structural properties at uniaxial tension; see Fig. 1(c, d, e).

2.2. Computational analysis

The meso-scale design influences the structural mechanical properties as well as the transport properties of the scaffolds, a dependence that was investigated through computational simulation. Given the structural design parameters, 3D descriptions of scaffold geometries were generated (ABAQUS 6.14 assembly module, Dassault Systemes, France), and thereafter used for FEA and CFD simulations.

2.2.1. Assessment of structural scaffold properties

Small-strain FEA was used to simulate structural scaffold properties. PCL was modeled as a linear elastic material with an elastic modulus of 345 MPa and a Poisson's ratio of 0.3 [68–70].

The cylindrical scaffold sample was compressed by d = 0.036 mm (corresponds to −1% strain) in the thickness direction between two rigid plates, while the quadratic sample was stretched by d = 0.098 mm (corresponds to 1% strain) along its axial direction between two rigid plates; see Fig. 1(c, d). A surface-to-surface contact model, with the frictional coefficient of 0.2, was used to prescribe the corresponding surface displacements in both compression and tension simulations. The distribution of stress and strain within the scaffold strands was calculated using the static Cauchy equation of motion (ABAQUS/Standard, Dassault Systemes, France). The computed reaction force F_R then defined the scaffold's effective compressive and tensile moduli

$$E = F_R/(A\varepsilon), \tag{2}$$

where $\varepsilon = 0.01$ denotes the average strain. Here, $A = \pi r^2 = 78.54\ \text{mm}^2$ and $A = ah = 35.28\ \text{mm}^2$ are the cross-sectional areas of the compression and tension model respectively.

2.2.2. Assessment of scaffold transport properties

The transport of water through the scaffold sample within a virtual bioreactor was simulated by CFD; see Fig. 1(c). Inlet and outlet tubes had a diameter of 2 mm, and a flow rate of $Q = 3.14 \times 10^{-4}\ \text{l} \cdot \text{s}^{-1}$ passed through the scaffold. This flow ensured the Reynolds number $Re \ll 1$ within the scaffold, and thus the validity of Darcy's law. A zero pressure was defined at the outlet, and the no-slip conditions were prescribed at all walls. Water was considered as a Newtonian fluid with a density of 1000 $\text{kg} \cdot \text{m}^{-3}$ and a dynamic viscosity of $\mu = 0.001\ \text{kg} \cdot \text{m}^{-1} \cdot \text{s}^{-1}$. The velocity and the pressure of the water throughout the model were then obtained by solving the continuity and Navier-Stokes equations (ABAQUS/CFD, Dassault Systemes, France).

Aside from the flow-induced wall shear stress (WSS) distribution over the strands, we also computed the average pressure drop ΔP between the top and bottom of the scaffold. This allowed us to determine the permeability coefficient using Darcy's law in the following equation

$$k = Q\mu L/(A\Delta P) \tag{3}$$

where $L = 3.6$ mm and $A = \pi r^2 = 78.54\ \text{mm}^2$ denote scaffold thickness and the cross-sectional area, respectively. Finally, the permeability coefficients were normalized $\bar{k} = k/k_{\text{ref}}$ by the permeability $k_{\text{ref}} = 9.13 \times 10^{-7}\ \text{m}^2$ of a hypothetical scaffold with 100% porosity.

2.3. Size exclusion chromatography (SEC)

The PCL filaments were purchased (3D4Makers, The Netherlands) and used as received. The average number molecular weight (Mn) and dispersity (Đ) of the PCL filament were characterized using size exclusion chromatography (SEC). The measurements were performed at 35 °C on a Viscotek GPCmax and autosampler (Malvern Panalytical, UK) equipped with an RI detector. The two linear mixed bead columns (LT4000L) and one guard column (TGuard) were used with $CHCl_3$ as the eluent (0.5 ml min^{-1}). Polystyrene standards with narrow dispersity were used for the calibration, and the flow rate fluctuations were corrected using toluene as an internal standard. For each sample, three repetitions were performed and the average of Mn and Đ reported.

2.4. Differential scanning calorimetry (DSC)

The polymers' thermal and viscoelastic properties are the major factors controlling the FFF-based 3D-printing process. The melting point (T_m) and crystallinity in % (X_c) were therefore characterized together with M_n and Đ of the PCL filaments prior to the setup of the 3D-printing process parameters. The thermal behavior of the PCL filament was evaluated using differential scanning calorimetry (DSC). A 100 μl aluminum pan was used and a DSC instrument (Mettle Toledo, USA) calibrated with indium. The measurement was conducted from 25 °C to 140 °C, with a heating rate of 10 °C min^{-1} and nitrogen flow of

Table 1
Description of the investigated scaffold designs formed by basic (B), gradient (G) and gradient and staggered (GS) meso-structures. Abbreviations: SD: strand diameter; SL: strand length; SO: strand orientation; SS: strand space.

Parameter / Type	SO, degree	SD, mm	SS, mm	No. of layers	Porosity, %	Top view	Side view of cross section
B	10	0.4	0.4	9	60.4		
	15	0.4	0.4			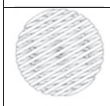	
	30	0.4	0.4			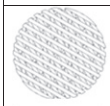	
	45	0.4	0.4			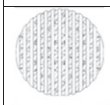	
	90	0.4	0.4			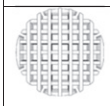	
	90a	0.4	0.8		73.5	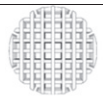	
	90b	0.4	1.2		77.9	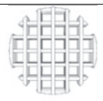	
G	15	0.4	1.2/1.2/0.8/0.8/0.4/0.8/0.8/1.2/1.2		75		
	90	0.4				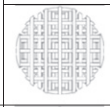	
GS	15	0.4			81.2		

50 ml min^{-1}. The peak T_m was taken from the first heating run, and the degree of X_c calculated from the enthalpy of fusion considering an infinitely large PCL crystal of 142 J g^{-1} [71], $X_c = [(\Delta H_m - \Delta H_c) / \Delta H_m^\circ] \times 100$.

2.5. Fabrication of PCL scaffolds

Given sets of representative meso-scale designs, scaffolds were manufactured for laboratory testing using a fifth generation MarkerBot Replicator Desktop 3D Printer (Stratasys, USA) [72] fitted with a 0.40 mm nozzle. PCL filaments of 1.75 mm in diameter were purchased and used as received (3DMakers, Netherlands). All geometrical files in stereolithography (STL) format were exported from Abaqus Assembly module, then sliced and converted to files using MakerBot Print (MakerBot Industries, USA).

2.6. Mechanical testing

Compression tests of 3D-printed scaffolds (B15, B90, G90, G15 and GS15) were conducted using an Instron 5566 (Instron, USA) tensile testing instrument equipped with a 10 kN load cell. Prior to testing, the printed samples were equilibrated for 24 h, and all tests were performed at room temperature and approximately 50% humidity. The scaffolds were compressed at a prescribed displacement rate of 0.35 mm s^{-1}. The force and the displacement were recorded throughout the testing, and thereafter converted to a first Piola-Kirchhoff stress versus engineering strain curve. Each scaffold was compressed by at least 1.5 mm, and the strain was then calculated with respect to this predefined configuration. The stress versus strain property of the scaffolds was non-linear: an initial progressive increase of stress is followed by an approximately linear stress versus strain response. In order to support the cross-comparison of such experimental data with the linear FEA simulations, we extracted a single elastic modulus from the compression experiments. The scaffold's compressive modulus was defined as the slope of the stress versus strain curve between strains of 0.05 and 0.1 ($n = 7$). At this strain level, the linear stress versus strain response has already been established.

2.7. Microcomputed tomography (μCT) characterization of scaffolds

All 3D-printed scaffolds were scanned using Skyscan 1172 system (Bruker Micro-CT, Belgium) at the spatial resolution of 9 μm. The

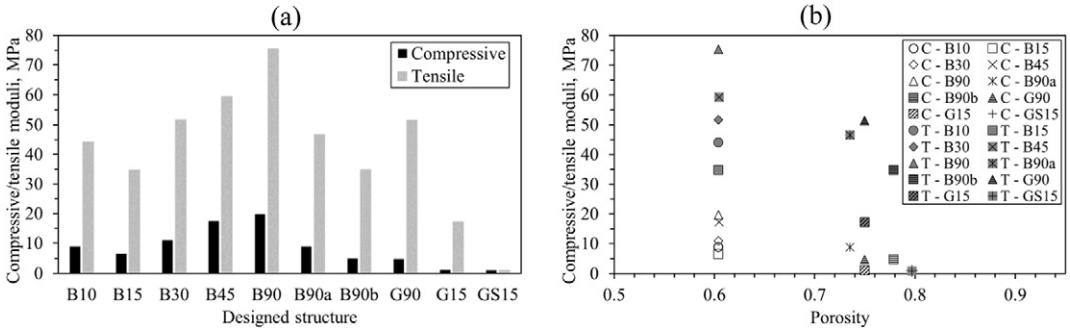

Fig. 2. Mechanical properties of scaffolds using basic (B), gradient (G), gradient and staggered (GS) meso-structures. (a) Finite element analysis-based (FEA-based) elastic moduli of scaffolds under compression and tension. (b) Relation between the compression/tension moduli and the porosity.

operation voltage was 40 kV, the current was 250 μA, and no filters were used. A step size of 0.4° and frame averaging of 2 was used. The reconstructions were based on the full cone beam Feldkamp reconstruction algorithm with automatically defined grayscale limits (NRecon, Bruker Micro CT, Belgium) [73]. The acquired CT images were analyzed to identify meso-structural features. For each scaffold, the region of interest (ROI) of 4 mm in radius was selected and automatically thresholded using the Otsu method. Surface area, total porosity, interconnectivity, mean pore size and pore size distribution were identified ($n = 3$), as well as 3D images of each meso-structure generated (CTAn and CTVox, Bruker Micro CT, Belgium).

2.8. Table top scanning electron microscope (SEM)

The five different scaffold designs 3D printed were analyzed to view the macro morphology using a table top scanning electron microscope (SEM) TM-1000 (Hitachi, Japan) with an acceleration voltage of 15 kV without conductive coating. Images were acquired at from a top and a cross-sectional view of scaffolds view following sectioning after immersion into liquid nitrogen. The images were taken at a magnification of 50×.

3. Results

3.1. Mechanical properties

Fig. 2(a) illustrates the FEA-based predictions of the elastic moduli *E* for the individual scaffolds under compression and tension, respectively. The scaffolds of G and GS meso-structures showed much softer properties in comparison with scaffolds using the B design meso-structure. Specifically, the GS15 design had a compression/tension modulus as low as 1.07/0.97 MPa, which is approximately 0.2% of the PCL filament's Young's modulus.

Fig. 2(b) shows the relation between the porosity and the compression/tension moduli. While higher porosity in average leads to lower moduli, scaffold designs of the same porosity may exhibit very different mechanical properties.

Fig. 3 shows a side view of the scaffolds under vertical compression. It presents the von Mises stress distribution in the PCL strands, color-coded in the range of 0.0 to 5.0 MPa. The images nicely illustrate the accumulation of stress, and thus the formation of stress columns, at the sites of structural communication between the top and bottom of the scaffolds. The more such columns develop, the stiffer the scaffold is.

Fig. 4(a) shows compressive stress-strain curves for scaffolds with basic (B15 and B90), gradient (G15 and G90), and gradient and staggered meso-structure (GS15). It is evident that higher stresses were formed for B15 and B90 scaffolds in comparison to that for G15, G90 and GS15 scaffolds during the whole compression testing. The clear difference in stress-strain curves indicate that the scaffold stiffness was significantly reduced by introducing gradient, gradient and staggered meso-structure designs (B90 > B15 > G90 > G15 > GS15). These stress-strain relations (B15 and B90) present the typical stress-stain curve for cellular solids under compression, with three regions, namely a linear region at small strains, a plateau of constant stress at moderate strains and a sharp increase region at large strains. Fig. 4(b) reports a comparison between experimentally acquired and computationally predicted compression moduli. Not all scaffolds were manufactured and only the ones shown in the figure underwent experimental testing. The FEA predictions were in good agreement with the experimental measurements, and the largest relative error of 16.5% was observed for the GS15 meso-structure design.

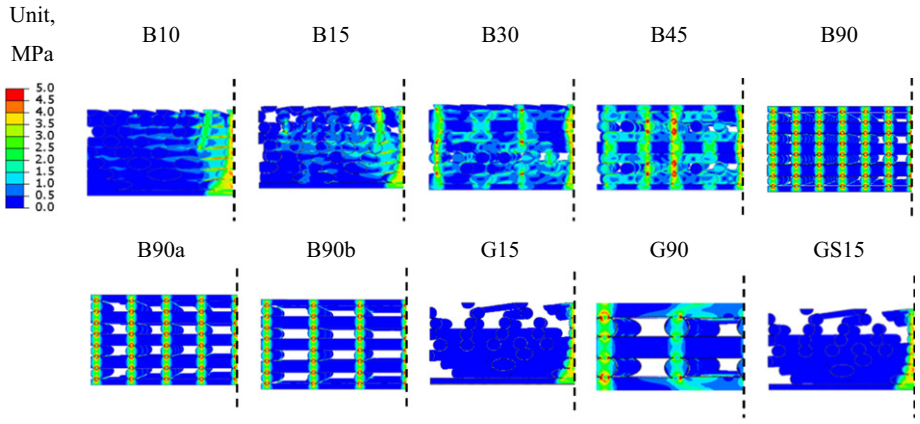

Fig. 3. Finite element analysis-based (FEA-based) prediction of the von Mises stress distribution in the strands of scaffolds using basic (B), gradient (G), gradient and staggered (GS) meso-structures. The scaffolds are under vertical compression, and the images represent the stress in the mid-cross section; the dotted line denotes the symmetry line.

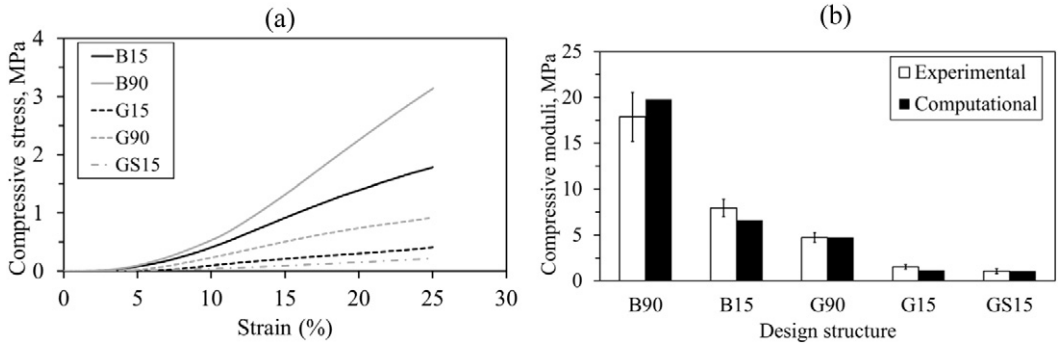

Fig. 4. (a) Representative stress – strain curves for scaffolds using basic (B), gradient (G), gradient and staggered (GS) meso-structures from compression testing, (b) experimentally measured and finite element analysis-based (FEA-based) compression moduli. The error bars show standard deviation of n = 7 experimental measurements.

3.2. Transport properties

Fig. 5 plots the relation of the normalized permeability $\bar{k}$ to the porosity of all investigated scaffolds. Given such a logarithmic representation, our results show a strong linear relation and confirm previous reports [74,75]. Moreover, the computed permeability values are in a reasonable range for tissue engineering applications when compared with other studies [75–78]. While the permeability only depends on the porosity, the individual scaffold design greatly influences the flow pattern that establishes within the scaffold. As shown in Fig. 6, the velocity inside a scaffold is much more homogeneous for the G and GS designs than it is for the B design.

Aside from the residence time, the flow-induced WSS within a scaffold is believed to be an important factor for the viability of cells in a perfusion bioreactor system [64]. Fig. 7 illustrates the WSS distribution as predicted by our CFD simulations. WSS is high in the central region of the scaffold and diminishes toward the edges. The different scaffold designs also led to very different WSS values, with higher WSS values for scaffolds of the B design (B15 and B90) than for the G and GS designs (G15, G90 and GS15).

3.3. Fabrication of 3D-printed scaffolds

Table 2 reports the parameters used for the 3D printing of PCL. The low T_m, the relatively low M_n and the wide Đ of our PCL filaments supported printing at temperatures as low as 100 °C without cooling of the printing plate. To cope with the relatively high viscoelasticity of the polymer, we used a printing speed as low as 10 mm·s^{-1}. Furthermore, a steady and continuous PCL filament extrusion was guaranteed by removing the retraction distance and avoiding stretching the highly flexible filament within the printer head. No infill, roof, floors, rafts or additional support structures were used. To allow for solidification of the polymer and increase the accuracy of the structure, 10 scaffolds were printed in parallel and the excess strands connecting the structures were cut away from the structures.

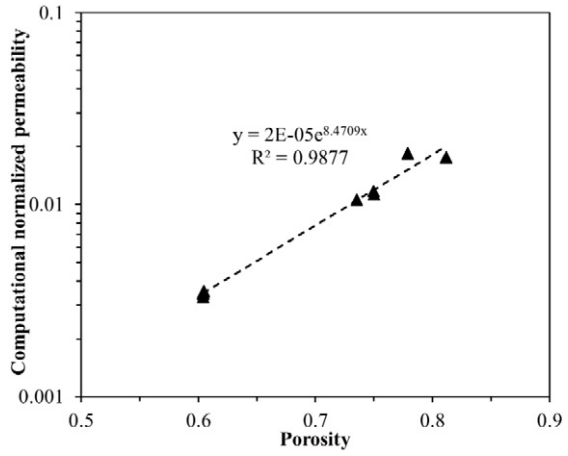

Fig. 5. Computational fluid dynamics-based (CFD-based) normalized permeability $\bar{k}$ versus porosity for all scaffolds.

3.4. Geometrical characterization of 3D-printed scaffolds

Figs. 8 and 9 demonstrate SEM and micro-CT images of 3D-printed PCL scaffolds with 5 different designs (B15, B90, G15, G90 and GS15), respectively. Both top and side views were provided. The manufactured samples successfully captured the imposed meso-structure of the B, G and GS designs. Strands from consecutive layers were well banded together, and the mean strand thickness was close to 0.4 mm for all manufactured scaffolds. The porosity of the manufactured scaffolds was also in good agreement with the imposed meso-structures. Table 3 reports full details in relation to the imposed design parameters.

Fig. 10 shows the distribution of pore size for the manufactured scaffolds, which was extracted from the micro-CT images. The scaffold designs B15 and B90 show a very inhomogeneous distribution in pore size, with approximately 0.4 mm being the dominating pore size. Given the gradient designs G15, G90 and GS15, the pore size is much more homogeneously distributed and forms a weak dominating size of approximately 0.9 mm. Table 3 reports additional pore-size data.

4. Discussion

This study explored the mechanical and transport properties of 3D-printed PCL-based scaffolds in relation their meso-structural design. The scaffolds were designed toward soft biological tissue applications, and methods such as FEA, CFD, experimental material characterization, SEC, DSC, and SEM and micro-CT imaging were used to acquire a holistic understanding of scaffold properties.

4.1. Mechanical properties

The FEA results showed that different meso-structure designs had a clear impact on mechanical scaffold properties. The compression/tension moduli of G and GS designs were much lower than those of the B designs. The porosity effect partially explains this; G and GS designs have a higher porosity than B designs. However, volume fraction is not the only influencing parameter in mechanical structural properties of scaffolds. While the B meso-structure scaffolds have identical theoretical porosity, their compression/tension moduli changed significantly from B10 to B90, with the B15 scaffold showing the lowest moduli. The porosity can also not explain the difference in stiffness between the G15 and G90 designs. All of this shows that, aside from the porosity, scaffold

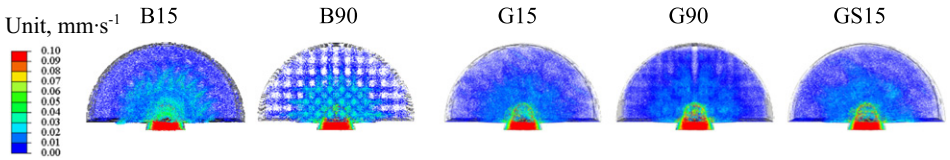

Fig. 6. Computational fluid dynamics-based (CFD-based) prediction of the fluid flow velocity inside the scaffolds of basic (B), gradient (G), gradient and staggered (GS) meso-structures. The image shows the scaffold as placed in a virtual bioreactor, and the color denotes the magnitude of the fluid flow velocity.

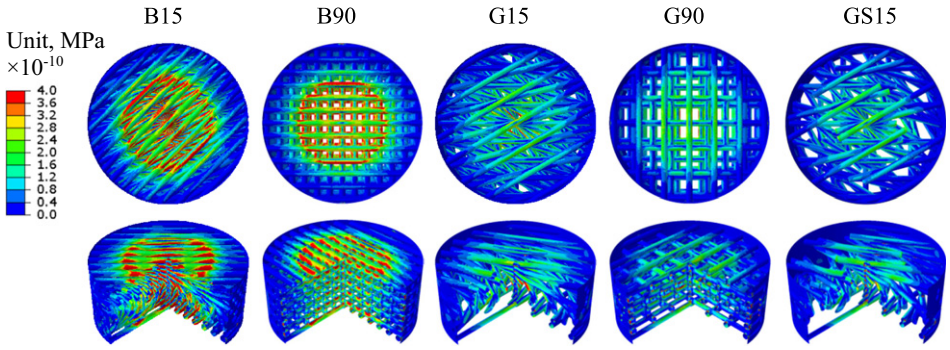

Fig. 7. Computational fluid dynamics-based (CFD-based) prediction of the wall shear stress (WSS) distribution inside the scaffolds of basic (B), gradient (G), gradient and staggered (GS) meso-structures. The image shows the scaffold as placed in a virtual bioreactor, and the color denotes the magnitude of the WSS vector.

stiffness is also greatly influenced by the individual strand configurations, an observation consistent with early studies [47,48].

Scaffold stiffness is greatly enhanced by direct mechanical communication, which accounts for the formation of stress bridges shown in Fig. 3. SO is one design parameter that directly influences the formation of stress bridges during scaffold compression; see the series of B designs. The G and GS designs led to a more homogenous distribution of stress than the B design meso-structure, which in turn resulted in fewer stress bridges and a lower scaffold stiffness. Furthermore, the stress-strain curves in Fig. 4a evidenced the difference between scaffolds with different designs under compression. Lower stresses were observed for scaffolds with the same meso-structure design when SO changes from 90 to 15 (i.e. B90 > B15, G90 > G15). Similarly, scaffolds with G and GS meso-structure designs resulted in lower compressive modulus and strength compared to scaffolds with B meso-structure design. These results are in consistence with the predicted stress distribution in Fig. 3. In addition, these stress-strain curves behaves similar to 3D printed PCL scaffolds under compression in other studies [35,69,79].

PCL-based scaffolds for soft biological tissue applications require a stiffness that is three orders of magnitude lower than the PCL filament's own stiffness. In our study, the GS15 design showed the lowest scaffold stiffness, closely matching the stiffness of the peripheral nerve (0.45 MPa), spiral cord tissue (0.2–0.8 MPa), fibrous tissue in breast (0.3 MPa), skin (0.3 MPa) and valves (1.1–1.3 MPa) [52–55,80]. A softer polymer or a smaller SD would naturally result in an even softer scaffold.

For most of our scaffolds, the stiffness was higher in tension than compression, with GS15 being the only exception. The staggered arrangement of strands avoided the direct mechanical communication (tension) along the strands, which in turn led to low tension stiffness. All the other designs supported the direct transmission of force along strands and led to tension stiffness that was several folds higher than of GS15.

We used linear FEA to investigate scaffold properties, a modeling assumption that could be seen as a limitation of our study. Especially under compression, the scaffolds showed non-linear stress versus strain response, a property that cannot be simulated by the linear FEA. While non-linear FEA would be possible, it requires more (uncertain) modeling assumptions, such as the description of the contact between the strands and a finite strain constitutive description of PCL.

The FEA-based prediction of compression stiffness of five scaffolds was validated against experimental data. With 16.5%, the G15 design showed the highest relative error in the validation, an error that could be a consequence of using linear FEA.

4.2. Transport properties

The CFD results demonstrated that the meso-structure influenced the scaffold's permeability, as well as the distribution of flow-induced WSS and velocity. While the design parameters had subtle influences on WSS and flow velocity, the scaffold permeability is solely determined by the porosity. Given a fixed pressure drop over the scaffold, the porosity determines the flow rate through the scaffold, and thus also the permeability, which is affected somewhat by the ratio between the flow rate and the pressure drop.

The Kozeny-Carman model has commonly been used in the literature to predict the theoretical permeability in porous media. One general form of Kozeny-Carman permeability equations is written as

Table 2
Characterization of the PCL filament together with parameters for 3D printing.

Parameter	T_m (°C)[a]	X_c (%)[a]	M_n[b] (kDa)	Đ[b]	Temperature (°C)[c]	Speed (mm s^{-1})[c]	Layer height (mm)[c]	Retraction distance (mm)[c]
PCL filament	60	49	104	1.5	100	10	0.4	0

[a] T_m and X_c of the filament determined by DSC in the first heating run.
[b] M_n and Đ as characterized by SEC, reported as an average of three repeats.
[c] Parameters used in the Makerbot replicator.

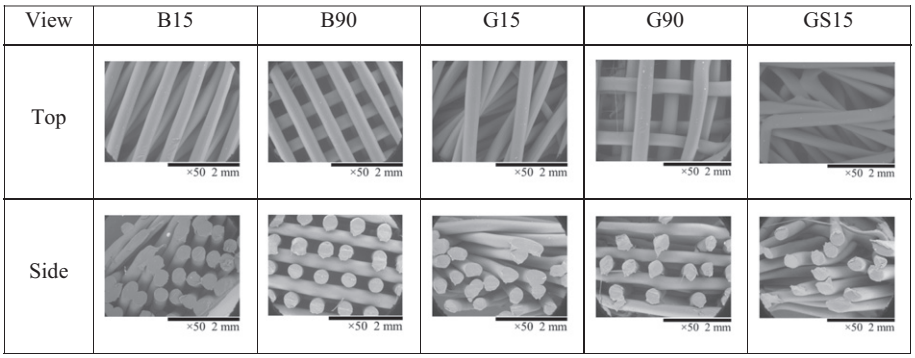

Fig. 8. Top and side views taken from SEM images of 3D-printed PCL scaffolds of basic (B), gradient (G), gradient and staggered (GS) meso-structures.

following [74,81]:

$$K = C_{k-c}\frac{p^3}{S_V^2} \tag{4}$$

where C_{k-c} is a non-dimensional constant, p is the porosity, and S_V is the specific surface area (the ratio of the surface to the volume). Taking the predicted permeability from CFD simulations into Eq. (4), the constant in the Kozeny-Carman equation, C_{k-c}, is calculated as a function of the porosity for all scaffold designs. As shown in Fig. 11, C_{k-c} relates to porosity in the fitted second-order polynomial manner. A constant value of 0.2 for C_{k-c} was reported by Lipowiecki et al. [82]. However, the present C_{k-c} – porosity relationship in Fig. 11 gives a better description and should be taken into account when estimating the theoretical permeability using the Kozeny-Carman model.

Although permeability is the most common parameter to specify the transport properties of a scaffold, it fails to provide detailed local hemodynamic conditions, and thus to describe the mechanical environment sensed by the cells within the scaffold. Fig. 6 illustrates the complex interaction between meso-structural design parameters and fluid flow velocity. Noticeable was the much more homogeneous velocity field for scaffolds based on G and GS designs as compared to scaffolds of the B design. A more homogenous velocity field might support a more even distribution of cells throughout the whole scaffold, and the majority of cells may potentially stay longer within the scaffold. This increases the likelihood of interaction with other cells and the surface of the scaffold, important factors for a biologically functioning scaffold.

A previous study concluded that a spatial gradient of pore size enhances cell-seeding efficiency and leads to a more uniform distribution of osteoblast-like cells [43]. Although we did not study the biological function of our scaffolds, it is interesting that our CFD simulations predicted hemodynamic conditions in G and GS meso-structures that could be beneficial for cell seeding. This point toward the positive biological effect of a spatial gradient in pore size.

The ability of a cell to attach to the scaffold depends on the local WSS level, a factor that strongly correlates with cell adhesion [63]. The presence of normal levels of shear stress is also important to cell activities, such as proliferation and differentiation [64]. The local WSS is directly influenced by the meso-structure, and thus it can be controlled by the scaffold design parameters. Our CFD simulations showed that the WSS in B designs was higher than in G and GS designs. Consequently, the G and GS designs might better support cell attachment within the scaffold than the B design.

4.3. Fabrication of 3D-printed scaffolds

3D-printing process parameters depend on the printing technology as well as the printing materials, and our study used FFF-based printing of PCL filaments. We optimized the printing temperature and speed in order to better replicate the scaffold meso-structure design during printing. However, ambient factors, such as temperature, also need to be carefully controlled toward achieving reproducible scaffold properties. Even minor variations in ambient factors can lead to inhomogeneous solidification of strands and other undesired outcomes.

4.4. Geometrical characterization of 3D-printed scaffolds

Geometrical features such as structure integrity, porosity, and pore size determine the behaviors of cells in scaffolds [9,59,83,84]. Top and cross-section views of printed scaffolds taken from SEM (Fig. 8) demonstrate that 3D structures with good interconnectivity were successfully fabricated for different designs. Delamination of layers was observed in some scaffolds (G90, GS15). This might be due to that two adhesive strands were separated from each other during specimen cutting. The layer-to-layer adhesion could be improved by tuning the printing parameters but this would also cause strands to fuse together and a lower scaffold porosity. While manufactured meso-structures will always differ from imposed designs, our micro-CT analysis showed that the porosity did not change by >10%. The alteration of the threshold levels to process the micro-CT images might have been enough to cause such an error. Another reason for this difference is related to the inherent principle of FFF printing: the formation of contact between strands decreases the total porosity of the scaffold.

While the pore size changed among the different designs, it was also more homogenously distributed for the G and GS designs than for the B design. The optimal pore size distribution of a scaffold changes for

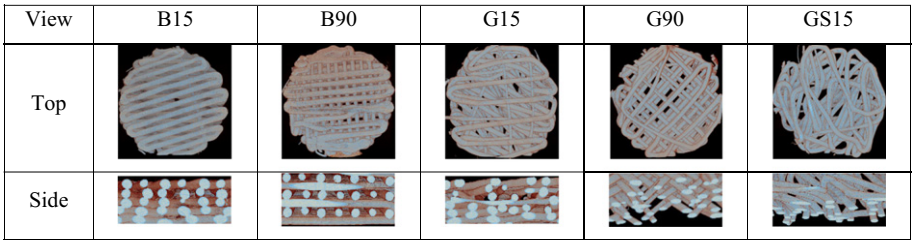

Fig. 9. Top and side views taken from micro-CT images of 3D-printed PCL scaffolds of basic (B), gradient (G), gradient and staggered (GS) meso-structures.

Table 3
Total porosity and pore size of 3D-printed PCL scaffolds with basic (B), gradient (G), gradient and staggered (GS) meso-structures. The data is based on the analysis of micro-CT images.

Scaffold design	Mean porosity, %	Standard deviation (n = 3)	Difference from design porosity, %	Mean pore size, mm	Standard deviation (n = 3)
B15	50.4	1.26	10	0.38	0.012
B90	54.7	0.73	5.7	0.41	0.015
G15	68.9	0.48	6.1	0.64	0.004
G90	70	1.50	5	0.69	0.053
GS15	75.6	0.23	5.6	0.81	0.016

different cell types, and most likely even for the same cell type at different stages of growth. In addition, a decrease in pore size leads to an increase in scaffold surface area, which is beneficial for initial cell attachment, while larger pores enhance the transport of nutrients and could be beneficial in the phase of cell growth and tissue regeneration. A spatial gradient in pore size might be a compromise between these two competing factors.

5. Conclusions

This study explored the suitability of 3D-printed PCL-based structures for soft biological tissue scaffolds. The scaffolds' meso-structures were designed toward low stiffness, and a mix of computational and experimental methods were used to examine the structures. Our results suggest that 3D printing of PCL-based structures is a fully feasible approach to manufacturing soft biological tissue scaffolds. Given their mechanical and transport properties, the GS meso-structure design is the most promising candidate among the designs explored in this study. The biological function of such designed scaffolds should be further studied in bioreactor and/or in-situ studies.

CRediT authorship contribution statement

Hailong Liu: Conceptualization, Methodology, Validation, Writing - original draft, Visualization, Formal analysis.**Astrid Ahlinder:** Methodology, Investigation, Writing - original draft.**Mohammed A. Yassin:** Investigation.**Anna Finne-Wistrand:** Conceptualization, Supervision.**T. Christian Gasser:** Conceptualization, Supervision, Writing - review & editing.

Declaration of competing interest

The authors declare that they no known competing financial interests or personal relationships that could have appeared to influence the work reported in this paper.

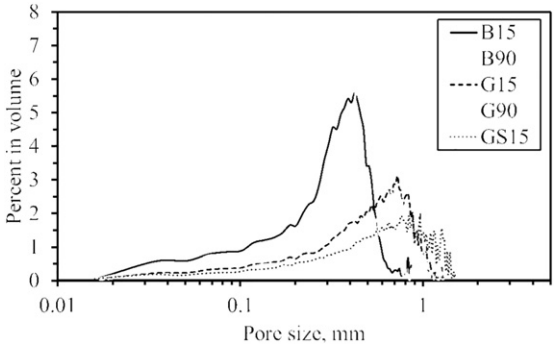

Fig. 10. Pore size distribution from the analysis of micro-CT images of 3D-printed PCL scaffolds with basic (B), gradient (G), gradient and staggered (GS) meso-structures.

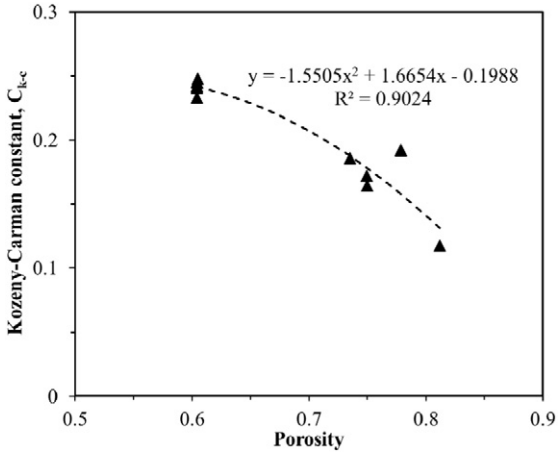

Fig. 11. Relationship between the constant of the Kozeny-Carman equation and porosity for different scaffold structures. A second-order polynomial fitting curve was given.

Acknowledgement

The authors acknowledge financial support from the Swedish Foundation for Strategic Research (RMA15-0010).

References

[1] D. Pappalardo, T. Mathisen, A. Finne-Wistrand, Biocompatibility of resorbable polymers: a historical perspective and framework for the future, Biomacromolecules 20 (2019) 1465–1477.
[2] J.P. Vacanti, R. Langer, Tissue engineering: the design and fabrication of living replacement devices for surgical reconstruction and transplantation, Lancet 354 (1999) 32–34.
[3] S.V. Murphy, A. Atala, 3D bioprinting of tissues and organs, Nat. Biotechnol. 32 (2014) 773–785.
[4] S.J. Hollister, Porous scaffold design for tissue engineering, Nat. Mater. 5 (2006) 590.
[5] D.W. Hutmacher, Scaffolds in tissue engineering bone and cartilage, Biomater. Silver Jubil. Compend. 21 (2006) 175–189.
[6] G.M. Cunniffe, P.J. Díaz-Payno, E.J. Sheehy, S.E. Critchley, H.V. Almeida, P. Pitacco, S.F. Carroll, O.R. Mahon, A. Dunne, T.J. Levingstone, C.J. Moran, R.T. Brady, F.J. O'Brien, P.A.J. Brama, D.J. Kelly, Tissue-specific extracellular matrix scaffolds for the regeneration of spatially complex musculoskeletal tissues, Biomaterials 188 (2019) 63–73.
[7] C.M. Nelson, M.J. Bissell, Of extracellular matrix, scaffolds, and signaling: tissue architecture regulates development, homeostasis, and cancer, Annu. Rev. Cell Dev. Biol. 22 (2006) 287–309.
[8] P.M. Crapo, T.W. Gilbert, S.F. Badylak, An overview of tissue and whole organ decellularization processes, Biomaterials 32 (2011) 3233–3243.
[9] C.M. Murphy, F.J. O'Brien, Understanding the effect of mean pore size on cell activity in collagen-glycosaminoglycan scaffolds, Cell Adhes. Migr. 4 (2010) 377–381.
[10] Y.C. Chai, A. Carlier, J. Bolander, S.J. Roberts, L. Geris, J. Schrooten, H. Van Oosterwyck, Current views on calcium phosphate osteogenicity and the translation into effective bone regeneration strategies, Acta Biomater. 8 (2012) 3876–3887.
[11] F.P.W. Melchels, A.M.C. Barradas, C.A. Van Blitterswijk, J. De Boer, J. Feijen, D.W. Grijpma, Effects of the architecture of tissue engineering scaffolds on cell seeding and culturing, Acta Biomater. 6 (2010) 4208–4217.
[12] I. Zein, D.W. Hutmacher, K.C. Tan, S.H. Teoh, Fused deposition modeling of novel scaffold architectures for tissue engineering applications, Biomaterials 23 (2002) 1169–1185.
[13] L.G. Bracaglia, B.T. Smith, E. Watson, N. Arumugasaamy, A.G. Mikos, J.P. Fisher, 3D printing for the design and fabrication of polymer-based gradient scaffolds, Acta Biomater. 56 (2017) 3–13.
[14] R.J. Mondschein, A. Kanitkar, C.B. Williams, S.S. Verbridge, T.E. Long, Polymer structure-property requirements for stereolithographic 3D printing of soft tissue engineering scaffolds, Biomaterials 140 (2017) 170–188.
[15] M.K. Włodarczyk-Biegun, A. del Campo, 3D bioprinting of structural proteins, Biomaterials 134 (2017) 180–201.
[16] F.P.W. Melchels, M.A.N. Domingos, T.J. Klein, J. Malda, P.J. Bartolo, D.W. Hutmacher, Additive manufacturing of tissues and organs, Prog. Polym. Sci. 37 (2012) 1079–1104.
[17] O.A. Mohamed, S.H. Masood, J.L. Bhowmik, Optimization of fused deposition modeling process parameters: a review of current research and future prospects, Adv. Manuf. 3 (2015) 42–53.
[18] S. Jain, T. Fuoco, M.A. Yassin, K. Mustafa, A.F. Wistrand, Printability and critical insight into polymer properties during direct- extrusion based 3D printing of medical grade polylactide and copolyesters, Biomacromolecules (2019) https://doi.org/10.1021/acs.biomac.9b01112.

[19] R. Schipani, D.R. Nolan, C. Lally, D.J. Kelly, Integrating finite element modelling and 3D printing to engineer biomimetic polymeric scaffolds for tissue engineering *Connect*, Tissue Res (2019) 8207.

[20] J. Aho, J.P. Bøtker, N. Genina, M. Edinger, L. Arnfast, J. Rantanen, Roadmap to 3D-printed oral pharmaceutical dosage forms: feedstock filament properties and characterization for fused deposition modeling, J. Pharm. Sci. 108 (2019) 26–35.

[21] C. Duty, C. Ajinjeru, V. Kishore, B. Compton, N. Hmeidat, X. Chen, P. Liu, A.A. Hassen, J. Lindahl, V. Kunc, What makes a material printable? A viscoelastic model for extrusion-based 3D printing of polymers, J. Manuf. Process. 35 (2018) 526–537.

[22] A. Ahlinder, T. Fuoco, Á. Morales-López, M.A. Yassin, K. Mustafa, A. Finne-Wistrand, Nondegradative additive manufacturing of medical grade copolyesters of high molecular weight and with varied elastic response, J. Appl. Polym. Sci. 48550 (2019) 18–20.

[23] L. Germain, C.A. Fuentes, A.W. van Vuure, A. des Rieux, C. Dupont-Gillain, 3D-printed biodegradable gyroid scaffolds for tissue engineering applications, Mater. Des. 151 (2018) 113–122.

[24] A.C. Albertsson, I.K. Varma, Recent developments in ring opening polymerization of lactones for biomedical applications, Biomacromolecules 4 (2003) 1466–1486.

[25] C.X.F. Lam, D.W. Hutmacher, J.T. Schantz, M.A. Woodruff, S.H. Teoh, Evaluation of polycaprolactone scaffold degradation for 6 months in vitro and in vivo, J. Biomed. Mater. Res. A 90 (2009) 906–919.

[26] T. Fuoco, A. Finne-Wistrand, Enhancing the properties of poly(ϵ-caprolactone) by simple and effective random copolymerization of ϵ-caprolactone with p-dioxanone, Biomacromolecules 20 (2019) 3171–3180.

[27] M. Bartnikowski, T.R. Dargaville, S. Ivanovski, D.W. Hutmacher, Degradation mechanisms of polycaprolactone in the context of chemistry, geometry and environment, Prog. Polym. Sci. 96 (2019) 1–20.

[28] W. Zhang, I. Ullah, L. Shi, Y. Zhang, H. Ou, J. Zhou, M.W. Ullah, X. Zhang, W. Li, Fabrication and characterization of porous polycaprolactone scaffold via extrusion-based cryogenic 3D printing for tissue engineering, Mater. Des. 180 (2019) 107946.

[29] F. Liu, C. Vyas, G. Poologasundarampillai, I. Pape, S. Hinduja, W. Mirihanage, P. Bartolo, Structural evolution of PCL during melt extrusion 3D printing, Macromol. Mater. Eng. 303 (2018) 1–6.

[30] J.H. Shim, J.H. Jeong, J.Y. Won, J.H. Bae, G. Ahn, H. Jeon, W.S. Yun, B.E. Bin, J.W. Choi, S.H. Lee, C.M. Jeong, H.Y. Chung, J.B. Huh, Porosity effect of 3D-printed polycaprolactone membranes on calvarial defect model for guided bone regeneration, Biomed. Mater. 13 (2018).

[31] K. Paul, S. Darzi, G. McPhee, M.P. Del Borgo, J.A. Werkmeister, C.E. Gargett, S. Mukherjee, 3D bioprinted endometrial stem cells on melt electrospun poly ε-caprolactone mesh for pelvic floor application promote anti-inflammatory responses in mice, Acta Biomater. 97 (2019) 162–176.

[32] S. Vijayavenkataraman, S. Thaharah, S. Zhang, W.F. Lu, J.Y.H. Fuh, Electrohydrodynamic jet 3D-printed PCL/PAA conductive scaffolds with tunable biodegradability as nerve guide conduits (NGCs) for peripheral nerve injury repair, Mater. Des. 162 (2019) 171–184.

[33] Y. Sun, A. Finne-Wistrand, A.C. Albertsson, Z. Xing, K. Mustafa, W.J. Hendrikson, D.W. Grijpma, L. Moroni, Degradable amorphous scaffolds with enhanced mechanical properties and homogeneous cell distribution produced by a three-dimensional fiber deposition method, J. Biomed. Mater. Res. - Part A 100 A (2012) 2739–2749.

[34] M.W. Naing, C.K. Chua, K.F. Leong, Y. Wang, Fabrication of customised scaffolds using computer-aided design and rapid prototyping techniques, Rapid Prototyp. J. 11 (2005) 249–259.

[35] N. Sudarmadji, J.Y. Tan, K.F. Leong, C.K. Chua, Y.T. Loh, Investigation of the mechanical properties and porosity relationships in selective laser-sintered polyhedral for functionally graded scaffolds, Acta Biomater. 7 (2011) 530–537.

[36] S.M. Giannitelli, D. Accoto, M. Trombetta, A. Rainer, Current trends in the design of scaffolds for computer-aided tissue engineering, Acta Biomater. 10 (2014) 580–594.

[37] S.J. Hollister, Porous scaffold design for tissue engineering, Nat. Mater. 4 (2005) 518–524.

[38] Z. Chen, Z. Su, S. Ma, X. Wu, Z. Luo, Biomimetic modeling and three-dimension reconstruction of the artificial bone, Comput. Methods Prog. Biomed. 88 (2007) 123–130.

[39] X.Y. Kou, S.T. Tan, A simple and effective geometric representation for irregular porous structure modeling, CAD Comput. Aided Des. 42 (2010) 930–941.

[40] S.C. Kapfer, S.T. Hyde, K. Mecke, C.H. Arns, G.E. Schröder-Turk, Minimal surface scaffold designs for tissue engineering, Biomaterials 32 (2011) 6875–6882.

[41] I. Maskery, L. Sturm, A.O. Aremu, A. Panesar, C.B. Williams, C.J. Tuck, R.D. Wildman, I.A. Ashcroft, R.J.M. Hague, Insights into the mechanical properties of several triply periodic minimal surface lattice structures made by polymer additive manufacturing, Polym. (United Kingdom) 152 (2017) 62–71.

[42] D. Valainis, P. Dondl, P. Foehr, R. Burgkart, S. Kalkhof, G.N. Duda, M. van Griensven, P.S.P. Poh, Integrated additive design and manufacturing approach for the bioengineering of bone scaffolds for favorable mechanical and biological properties, Biomed. Mater. 14 (2019) 65002.

[43] J.M. Sobral, S.G. Caridade, R.A. Sousa, J.F. Mano, R.L. Reis, Three-dimensional plotted scaffolds with controlled pore size gradients: effect of scaffold geometry on mechanical performance and cell seeding efficiency, Acta Biomater. 7 (2011) 1009–1018.

[44] S. Gómez, M.D. Vlad, J. López, E. Fernández, Design and properties of 3D scaffolds for bone tissue engineering, Acta Biomater. 42 (2016) 341–350.

[45] A.A. Zadpoor, Bone tissue regeneration: the role of scaffold geometry, Biomater. Sci. 3 (2015) 231–245.

[46] T.B.F. Woodfield, J. Malda, J. De Wijn, F. Péters, J. Riesle, C.A. Van Blitterswijk, Design of porous scaffolds for cartilage tissue engineering using a three-dimensional fiber-deposition technique, Biomaterials 25 (2004) 4149–4161.

[47] L. Moroni, J.R. De Wijn, C.A. Van Blitterswijk, 3D fiber-deposited scaffolds for tissue engineering: influence of pores geometry and architecture on dynamic mechanical properties, Biomaterials 27 (2006) 974–985.

[48] D.W. Hutmacher, T. Schantz, I. Zein, K.W. Ng, S.H. Teoh, K.C. Tan, Mechanical properties and cell cultural response of polycaprolactone scaffolds designed and fabricated via fused deposition modeling, J. Biomed. Mater. Res. 55 (2) (2001) 203–216.

[49] J.A. Stella, A. D'Amore, W.R. Wagner, M.S. Sacks, On the biomechanical function of scaffolds for engineering load-bearing soft tissues, Acta Biomater. 6 (2010) 2365–2381.

[50] E.C. Clarke, S. Cheng, L.E. Bilston, The mechanical properties of neonatal rat spinal cord in vitro, and comparisons with adult, J. Biomech. 42 (2009) 1397–1402.

[51] T.C. Gasser, R.W. Ogden, G.A. Holzapfel, Hyperelastic modelling of arterial layers with distributed collagen fibre orientations, J. R. Soc. Interface 3 (2006) 15–35.

[52] I.P. Herman, Physics of the Human Body, Springer, 2007.

[53] M.Z. Albanna, T.H. Bou-Akl, H.L. Walters, H.W.T. Matthew, Improving the mechanical properties of chitosan-based heart valve scaffolds using chitosan fibers, J. Mech. Behav. Biomed. Mater. 5 (2012) 171–180.

[54] J. LeMaitre, Handbook of Materials Behavior Models, Three-volume Set: Nonlinear Models and Properties, Academic Press, 2001.

[55] T.K. Hung, G.L. Chang, H.S. Lin, F.R. Walter, L. Bunegin, Stress-strain relationship of the spinal cord of anesthetized cats, J. Biomech. 14 (1981) 269–276.

[56] T.A. Krouskop, T.M. Wheeler, F. Kallel, B.S. Garra, T. Hall, Elastic moduli of breast and prostate tissues under compression, Ultrason. Imaging 20 (1998) 260–274.

[57] I. Bružauskaitė, D. Bironaitė, E. Bagdonas, E. Bernotienė, Scaffolds and cells for tissue regeneration: different scaffold pore sizes—different cell effects, Cytotechnology 68 (2016) 355–369.

[58] R.A. Perez, G. Mestres, Role of pore size and morphology in musculo-skeletal tissue regeneration, Mater. Sci. Eng. C 61 (2016) 922–939.

[59] C.M. Murphy, M.G. Haugh, F.J. O'Brien, The effect of mean pore size on cell attachment, proliferation and migration in collagen-glycosaminoglycan scaffolds for bone tissue engineering, Biomaterials 31 (2010) 461–466.

[60] H.A. Declercq, T. Desmet, P. Dubruel, M.J. Cornelissen, The role of scaffold architecture and composition on the bone formation by adipose-derived stem cells, Tissue Eng. Part A 20 (2014) 434–444.

[61] Y. Chen, S. Zhou, Q. Li, Microstructure design of biodegradable scaffold and its effect on tissue regeneration, Biomaterials 32 (2011) 5003–5014.

[62] J.M. Kemppainen, S.J. Hollister, Differential effects of designed scaffold permeability on chondrogenesis by chondrocytes and bone marrow stromal cells, Biomaterials 31 (2010) 279–287.

[63] F.P.W. Melchels, B. Tonnarelli, A.L. Olivares, I. Martin, D. Lacroix, J. Feijen, D.J. Wendt, D.W. Grijpma, The influence of the scaffold design on the distribution of adhering cells after perfusion cell seeding, Biomaterials 32 (2011) 2878–2884.

[64] D.W. Hutmacher, H. Singh, Computational fluid dynamics for improved bioreactor design and 3D culture, Trends Biotechnol. 26 (2008) 166–172.

[65] Y. Guyot, F.P. Luyten, J. Schrooten, I. Papantoniou, L. Geris, A three-dimensional computational fluid dynamics model of shear stress distribution during neotissue growth in a perfusion bioreactor, Biotechnol. Bioeng. 112 (2015) 2591–2600.

[66] S.H. Oh, I.K. Park, J.M. Kim, J.H. Lee, In vitro and in vivo characteristics of PCL scaffolds with pore size gradient fabricated by a centrifugation method, Biomaterials 28 (2007) 1664–1671.

[67] S.H. Oh, T.H. Kim, I.G. Il, J.H. Lee, Investigation of pore size effect on chondrogenic differentiation of adipose stem cells using a pore size gradient scaffold - biomacromolecules (ACS Publications), Am. Chem. Soc. 11 (2010) 1948–1955.

[68] S. Eshraghi, S. Das, Micromechanical finite-element modeling and experimental characterization of the compressive mechanical properties of polycaprolactone-hydroxyapatite composite scaffolds prepared by selective laser sintering for bone tissue engineering, Acta Biomater. 8 (2012) 3138–3143.

[69] J.F.M. Ribeiro, S.M. Oliveira, J.L. Alves, A.J. Pedro, R.L. Reis, E.M. Fernandes, J.F. Mano, Structural monitoring and modeling of the mechanical deformation of three-dimensional printed poly(ϵ-caprolactone) scaffolds, Biofabrication 9 (2017).

[70] H. Gao, X. Li, C. Wang, P. Ji, C. Wang, Mechanobiologically optimization of a 3D titanium-mesh implant for mandibular large defect: a simulated study, Mater. Sci. Eng. C 104 (2019) 109934.

[71] Y. Ikada, H. Tsuji, Biodegradable polyesters for medical and ecological applications, Macromol. Rapid Commun. 21 (2005) 117–132.

[72] A. Ahlinder, T. Fuoco, A. Finne-Wistrand, Medical grade polylactide, copolyesters and polydioxanone: rheological properties and melt stability, Polym. Test. 72 (2018) 214–222.

[73] M.A. Yassin, K.N. Leknes, Y. Sun, S.A. Lie, A. Finne-Wistrand, K. Mustafa, Surfactant tuning of hydrophilicity of porous degradable copolymer scaffolds promotes cellular proliferation and enhances bone formation, J. Biomed. Mater. Res. - Part A 104 (2016) 2049–2059.

[74] H. Montazerian, M. Zhianmanesh, E. Davoodi, A.S. Milani, M. Hoorfar, Longitudinal and radial permeability analysis of additively manufactured porous scaffolds: effect of pore shape and porosity, Mater. Des. 122 (2017) 146–156.

[75] A. Syahrom, M.R. Abdul Kadir, M.N. Harun, A. Öchsner, Permeability study of cancellous bone and its idealised structures, Med. Eng. Phys. 37 (2015) 77–86.

[76] M.R. Dias, P.R. Fernandes, J.M. Guedes, S.J. Hollister, Permeability analysis of scaffolds for bone tissue engineering, J. Biomech. 45 (2012) 938–944.

[77] C.G. Jeong, S.J. Hollister, Mechanical, permeability, and degradation properties of 3D designed poly(1,8 octanediol-co-citrate) scaffolds for soft tissue engineering, J. Biomed. Mater. Res. - Part B Appl. Biomater. 93 (2010) 141–149.

[78] A. Rahbari, H. Montazerian, E. Davoodi, S. Homayoonfar, Predicting permeability of regular tissue engineering scaffolds: scaling analysis of pore architecture, scaffold length, and fluid flow rate effects, Comput. Methods Biomech. Biomed. Engin. 20 (2017) 231–241.

[79] D.R. Fonseca, R. Sobreiro-Almeida, P.C. Sol, N.M. Neves, Development of non-orthogonal 3D-printed scaffolds to enhance their osteogenic performance, Biomater. Sci. 6 (2018) 1569–1579.
[80] B.S. Garra, F. Kallel, T.M. Wheeler, T.A. Krouskop, T. Hall, Elastic moduli of breast and prostate tissues under compression, Ultrason. Imaging 20 (2013) 260–274.
[81] P.F. Egan, V.C. Gonella, M. Engensperger, S.J. Ferguson, K. Shea, Computationally designed lattices with tuned properties for tissue engineering using 3D printing, PLoS One 12 (2017) 1–20.
[82] M. Lipowiecki, M. Ryvolová, Á. Töttösi, N. Kolmer, S. Naher, S.A. Brennan, M. Vázquez, D. Brabazon, Permeability of rapid prototyped artificial bone scaffold structures, J. Biomed. Mater. Res. - Part A 102 (2014) 4127–4135.
[83] G.N. Van, L. Geris, G. Carmeliet, O.H. Van, Size does matter: an integrative in vivo-in silico approach for the treatment of critical size bone defects, PLoS Comput. Biol. 10 (2014) e1003888.
[84] Q. Yao, J.G.L. Cosme, T. Xu, J.M. Miszuk, P.H.S. Picciani, H. Fong, H. Sun, Three dimensional electrospun PCL/PLA blend nanofibrous scaffolds with significantly improved stem cells osteogenic differentiation and cranial bone formation, Biomaterials 115 (2017) 115–127.